Quantum computation of mass gap in an asymptotically free theory

Paulo F. Bedaque,[1, *] Edison M. Murairi,[2, 3, †] Gautam Rupak,[4, ‡] and Valery S. Simonyan[1, §]

[1]*Department of Physics, University of Maryland, College Park, MD 20742, USA*
[2]*Superconducting and Quantum Materials System Center (SQMS), Batavia, Illinois, 60510, USA.*
[3]*Fermi National Accelerator Laboratory, Batavia, Illinois, 60510, USA*
[4]*Department of Physics & Astronomy and HPC² Center for Computational Sciences,*
Mississippi State University, Mississippi State, MS 39762, USA

In relativistic field theories, the mass spectrum is given by the difference between the energy of the vacuum and the excited states. Near the continuum limit, the cancellation between these two values leads to loss of precision. We propose a method to extract the mass gap directly using quantum computers and apply it to a particular version of the nonlinear σ-model with the correct continuum limit and perform calculations in quantum hardware (at strong coupling) and simulation in classical computers (at weak coupling).

Keywords: mass gap, sigma model, asymptotic freedom, quantum computation

I. INTRODUCTION

A central challenge in computational Quantum Chromodynamics (QCD), and in numerical quantum field theory in general, is the first-principles calculation of physically important but inaccessible observables within the standard lattice formulation. The Euclidean path integral approach, while highly successful for a wide range of zero-density and static quantities, encounters a fundamental obstruction known as the sign problem when a finite baryon chemical potential is introduced to study dense matter. The ensuing complex action prevents efficient Monte Carlo sampling, precluding ab initio exploration of the QCD phase diagram at high density. A related, and equally profound, challenge is the calculation of real-time observables. Key quantities such as transport coefficients, scattering amplitudes, and parton distribution functions are defined in Minkowski spacetime and cannot be directly extracted from imaginary-time lattice correlators without an ill-posed analytic continuation.

Quantum computations of QCD observables would in principle avoid the aforementioned problems by directly performing the calculations in Minkowski space using unitary time evolution with the Hamiltonian. Formulating QCD and other quantum field theories in a form amenable to quantum computation, as well as developing practical algorithms for their simulation, is a very active field of research. In one approach, the bosonic fields are truncated in the Fourier basis [1–8] or a mixed basis [9]. In another approach, the underlying continuous symmetry group is replaced with a discrete subgroup [10–18]. Other methods include a fuzzy regulation [19–21], quantum link models [22–24]. A common framework for these calculations involves a multi-stage process: the first is encoding the theory's degrees of freedom into a quantum register; second, preparing the ground state (or a close approximation of it); third, implementing time evolution generated by the Hamiltonian in terms of quantum gates; and finally, measuring the relevant observables. Significant theoretical challenges are inherent to each of these steps, presenting obstacles above and beyond the challenging engineering problem of building large, fault-tolerant quantum computers.

In this work, we address the challenge of computing a fundamental property of strongly-coupled field theories—the mass gap—using a quantum computer. As a concrete testbed for our method, we employ the (1+1)-dimensional nonlinear $O(3)$ σ-model. This theory provides an ideal proving ground, as it shares key nonperturbative features with QCD, namely asymptotic freedom and dynamical mass generation, while being more amenable to initial simulations on current quantum hardware. For that, some issues have to be addressed. The first, already tackled in [19, 20, 25–28], arises from the fact that this theory contains bosonic fields, with an infinite number of degrees of freedom at each space-time point, which cannot be accommodated in a finite quantum register. This problem was solved by finding a theory that can be encoded in a finite number of qubits per lattice site (only 2 in fact) which, nevertheless, belongs to the same universality class as the full bosonic $O(3)$ nonlinear σ-model. This theory, referred to as the "fuzzy σ-model" [19, 20, 25] or the "Heisenberg comb" [26–28] is what we simulated in a quantum computer. The second issue we address comes from the fact that the mass gap (the mass of the lightest particle) in lattice units approaches zero in the continuum limit. Computing this number accurately from the difference between the *approximate* values of the much larger ground and the first excited state energies E_0, E_1 is a difficult feat leading to a severe loss of precision. We suggest, implement, and test a way around this problem.

---

* bedaque@umd.edu
† emurairi@fnal.gov
‡ grupak@ccs.msstate.edu
§ vsimon24@umd.edu

II.   THE FUZZY $O(3)$ σ-MODEL

For applications in quantum computing, field theories are most naturally formulated in the Hamiltonian framework. Thus, we will start briefly reviewing the (regular, non-"fuzzy") $1+1$ dimensional $O(3)$ nonlinear σ-model in that language. Consider a one-dimensional spatial lattice of L sites separated by a lattice spacing a. At each site x, the local Hilbert space of the model consists of square-integrable functions over the unit sphere S^2, $\psi(\mathbf{n})$, $\mathbf{n}^2 = 1$. These functions can be expanded in an infinite series of $\mathbf{n}$ as

$$\psi(\mathbf{n}) = \psi_0 + \psi_i \mathbf{n}_i + \psi_{ij} \mathbf{n}_i \mathbf{n}_j + \cdots , \qquad (1)$$

where $\mathbf{n}_i$ are the components of $\mathbf{n}$. The full Hilbert space is the tensor product over all sites. The field operators $\mathbb{n}_i(x)$ act by multiplication: $\mathbb{n}_i(x)\psi = \mathbf{n}_i(x)\psi$. Global $O(3)$ rotations act as $\mathbb{R}\psi(\{\mathbf{n}(x)\}) = \psi(\{R^{-1}\mathbf{n}(x)\})$ and are generated by angular momentum operators $\mathbb{T}_k$. The on-site algebra satisfies

$$\begin{aligned}
[\mathbb{n}_i, \mathbb{n}_j] &= 0 \,, \\
[\mathbb{T}_i, \mathbb{T}_j] &= i\epsilon_{ijk}\mathbb{T}_k \,, \\
[\mathbb{T}_i, \mathbb{n}_j] &= i\epsilon_{ijk}\mathbb{n}_k \,.
\end{aligned} \qquad (2)$$

The unit norm constraint is enforced as restriction on the Hilbert space:

$$\left[\mathbb{n}(x)^2 - \mathbb{1} \right] \psi = 0 \,, \qquad (3)$$

and the Hamiltonian is given by [29] [1]:

$$a\mathbb{H} = \eta g^2 \sum_x \mathbb{T}(x)^2 - \frac{\eta}{g^2} \sum_x \mathbb{n}(x) \cdot \mathbb{n}(x+1) \,, \quad (4)$$

is a sum of a "kinetic" term and a nearest-neighbor "potential" energy. Here a is the spatial lattice spacing and η and g^2 two parameters controlling the strength of each term.

The coefficients in Eq. (4) were parametrized in order to make its eigenstates (and, consequently, the correlation length ξ) independent of η, while energies are simply proportional to it. Lorentz invariance is restored by tuning η so the energy gap $E_1 - E_0$ equals the mass of the lightest particle $m = 1/\xi$. The continuum limit ($\xi \gg a$) is obtained by setting $g(a) \to 0$ as $a \to 0$ according to

$$\frac{dg(a)}{d\log a} = b_0 g^2(a) \,, \qquad (5)$$

where b_0 is a known numerical constant [30]. Since the energy gap is independent of a in the continuum limit, it must have the form

$$m \sim \frac{1}{a} \exp\left[-\frac{1}{2b_0 g^2(a)} \right] \,. \qquad (6)$$

In the continuum limit the nonlinear model is solvable and it describes a triplet of particles of mass interacting through a δ-function interaction [31]. Usually, one sets the value of $g(a)$ at a particular value of $a = \bar{a}$ by demanding that the experimentally known particle mass m is reproduced. After fixing $g(\bar{a})$, all other observables can be computed, a procedure known as "scale setting".

The Hilbert space of this theory is infinite dimensional even if L is finite. Therefore, its states cannot be encoded in a finite quantum register, a feature shared by all bosonic field theories. Therefore, it is necessary to truncate not only space (that is what the lattice regularization does), but also *field* space (in this case the unit sphere), a process sometimes called "qubitization". Various qubitizations of the σ-model have been proposed. One is to substitute the unit sphere S^2 by the vertices of one of the Platonic solids, in order to maintain as much of the rotation symmetry as possible. The resulting model, however, does not have a continuum limit [32–34]. Another possibility is to expand the wavefunction at each site into spherical harmonics but truncate the series to $\ell \leq \ell_{\max}$ [29]. Despite keeping the full rotation invariance, the resulting model also lacks a continuum limit for fixed $\ell_{\max}$, as shown in [19]. But a qubitization with the proper continuum limit exists. It was originally [25] inspired by a construction in non-commutative geometry, the "fuzzy sphere" [35, 36] and, at the same time, by very different considerations [37]. Further studies using Monte Carlo and tensor network methods [20, 27, 38] established that the continuum limit of the fuzzy model is asymptotically free and indeed coincides with regular σ-model defined by Eq. (4). The fuzzy σ-model is defined by choosing an irreducible representation j of the symmetry group $SU(2)$. For simplicity here, we will choose $j = 1/2$. The Hilbert space of the regular σ-model is substituted by the (finite dimensional) space of 2×2 matrices.[2] The analogue of Eq. (1) is the finite expansion $\Psi = \psi_0 \mathbb{1} + \psi_k \sigma_k$, where $\sigma_k = (X, Y, Z)$ are the Pauli matrices, is the finite-dimensional.

The operators $\mathfrak{n}_k = \frac{1}{\sqrt{3}}\sigma_k$ and $\mathcal{T}_k = \frac{1}{2}[\sigma_k, \cdots]$ are the fuzzy analogues of $\mathbb{n}_k, \mathbb{T}_k$ and satisfy

$$\mathfrak{n}^2 = \mathbb{1} \,, \qquad\qquad [\mathfrak{n}_i, \mathfrak{n}_j] = \frac{2}{\sqrt{3}}\epsilon_{ijk}\mathfrak{n}_k \,,$$

$$[\mathcal{T}_i, \mathcal{T}_j] = i\epsilon_{ijk}\mathcal{T}_k \,, \qquad [\mathcal{T}_i, \mathfrak{n}_j] = i\epsilon_{ijk}\mathfrak{n}_k \,. \qquad (7)$$

Except for the commutation relation among the $\mathfrak{n}_i$, those are the same as in Eq. (2). This is the sense in which the unit sphere of the σ-model was substituted by a non-commutative manifold [3]. The Hamiltonian of the fuzzy

---

[1] We use units where $\hbar = 1 = c$.

[2] One can also use the generators of larger irreps. and a correspondingly larger Hilbert space.

[3] Note that it is the field space that is non-commutative, not the spacetime as in a completely different class of theories extensively studied [39].

model is the analogue of Eq. (4):

$$aH = \eta g^2 \sum_x \mathcal{T}(x)^2 + \frac{\eta}{g^2} \sum_x \mathfrak{n}(x) \cdot \mathfrak{n}(x+1) . \quad (8)$$

Notice the sign change between Eq. (4) and Eq. (8): the nearest-neighbor interaction in Eq. (8) is antiferromagnetic. It is convenient to expand the wavefunction at every site as $\Psi = \psi_\mu E_\mu$ with

$$e_0 = \begin{bmatrix} 1 & 0 \\ 0 & 0 \end{bmatrix}, e_1 = \begin{bmatrix} 0 & 1 \\ 0 & 0 \end{bmatrix}, e_2 = \begin{bmatrix} 0 & 0 \\ 1 & 0 \end{bmatrix}, e_3 = \begin{bmatrix} 0 & 0 \\ 0 & 1 \end{bmatrix}. \quad (9)$$

After a further conjugation with $\mathbb{1} \otimes \sigma_2$ at each site we arrive at the following form for the Hamiltonian (this is in the form used in [27]):

$$aH = \frac{\eta g^2}{2} \sum_{l=0}^{L-1} [X_{2l+1}X_{2l} + Y_{2l+1}Y_{2l} + Z_{2l+1}Z_{2l}]$$
$$+ \frac{\eta}{3g^2} \sum_{l=0}^{L-1} [X_{2l+2}X_{2l} + Y_{2l+2}Y_{2l} + Z_{2l+2}Z_{2l}], \quad (10)$$

where periodic boundary condition in the second summation of terms is implied. This Hamiltonian differs from the one in Eq. (8) only by a term proportional to the identity that just shifts the energy eigen values without affecting the gap or the eigen vectors. Equation Eq. (10) can be visualized using the schematic in Fig. 1 [27], where the even and odd qubits—labeled the "head" (squares) and "fuzz" (circles) respectively—are coupled via single and double lines representing the anti-ferromagnetic couplings in the potential and kinetic terms, respectively.
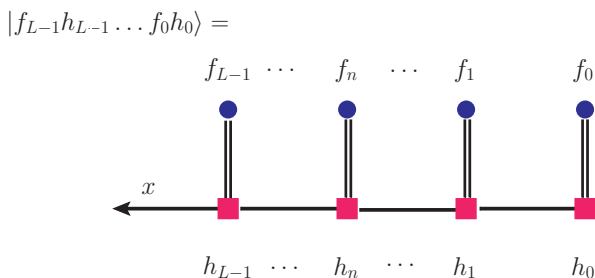

FIG. 1. Diagram depicting the "Heisenberg comb" form of the fuzzy σ-model [27]. The "head" qubits are denote by h_n (red squares) and the "fuzz" qubits are denoted by f_n (blue circles) at site $l = 0, 1, \ldots, L-1$.

The model defined by Eq. (10) is easily understood in two limits. First, in the strong coupling limit $g \to \infty$, only the kinetic term survives and the ground state factorizes into a tensor product of singlets at each site:

$$|\Psi_{\text{strong}}\rangle = \bigotimes_{l=0}^{L-1} \frac{|0_{2l+1}1_{2l}\rangle - |1_{2l+1}0_{2l}\rangle}{\sqrt{2}}, \quad (11)$$

where $|q_l\rangle$ with $q_l = 0, 1$ correspond to the state of the l-th qubit. Conversely, in the weak coupling limit $g \to 0$, the potential term dominates. In this limit, the fuzz qubits completely decouple and the ground state has a 2^L-fold degeneracy corresponding to all possible states of the fuzz qubits. In fact, all states of the form $|\Psi\rangle = |\text{antiferro}\rangle \otimes |\text{any}\rangle$, where $|\text{antiferro}\rangle$ is the ground state of the Heisenberg antiferromagnetic chain among the head qubits and $|\text{any}\rangle$ being any state of the fuzz qubits, are degenerate in the weak coupling limit. The kinetic term lifts this degeneracy only at second order in perturbation theory [21]. We find that, of all states of this form, the state that smoothly connects to the ground state at non-zero g is

$$|\Psi_{\text{weak}}\rangle = |\text{antiferro}\rangle \otimes |\text{antiferro}\rangle . \quad (12)$$

As explained in Ref. [21], perturbing the ground state $|\psi_{\text{weak}}\rangle$ in Eq. (12) with the kinetic term to obtain the weak coupling expansion series leads to infrared divergences as $L \to \infty$, a hallmark of asymptotically free theories.

III. MEASURING THE GAP

In all relativistic field theories, the energy of the ground state has no physical meaning. The interest is instead on observables like the mass of the lightest particle, given by the energy gap between the ground and the first excited state. This poses a challenge to quantum computation. Near the continuum limit, the ground state energy E_0 and the excited state energy (or degenerate energies) E_1 are of the order of the inverse lattice spacing $\sim 1/a$ while their difference $\omega = E_1 - E_0$ is much smaller $\omega \sim a^0$. Any *approximate* determination of the individual state energies leads to large deviations in the mass gap. In this work, we introduce a paradigm that avoids this pitfall by constructing an observable for measuring the mass gap directly. Suppose we setup a linear combination of the ground $|E_0\rangle$ and first excited $|E_1\rangle$ states, respectively, as an initial condition:

$$|\Psi(0)\rangle = \alpha |E_0\rangle + i\beta |E_1\rangle . \quad (13)$$

At later times, the expectation value of the operator $d = |E_0\rangle \langle E_1| + |E_1\rangle \langle E_0|$ connecting these two states is given by

$$\langle \Psi(t)| d |\Psi(t)\rangle = -2\alpha\beta \sin(mt) , \quad (14)$$

where α, β are assumed to be real. Therefore, measuring $\langle d \rangle$ as a function of time gives the value of the mass gap directly, bypassing the delicate cancellation between E_1 and E_0. Of course, knowing the states $|E_0\rangle, |E_1\rangle$ amounts to solving the theory. The practical strategy is to have a rough approximation of these states so the oscillations in $\langle d \rangle$ are dominated by Eq. (14). Other, higher frequency oscillations, can be filtered out by a number of

techniques as long as their amplitude is not too large, as we will demonstrate below. We refer to d as the dipole operator, as it is reminiscent of an electric dipole transition operator connecting states with opposite parity, in this case singlet and triplet states.

Note that the expectation value of any operator that does not commute with the Hamiltonian H would show oscillations corresponding to the various relative phases associated with energy differences in a superposition state of energy eigenstates. To see a clear signal of the oscillation due to $m = E_1 - E_0$, an initial state composed mostly of $|E_0\rangle, |E_1\rangle$ states, and an operator mostly coupling these states is preferable.

In the strong coupling region $g \gtrsim 1$ we approximate the ground state by its strong coupling limit (Eq. (11)):

$$|E_0\rangle \approx |\Psi_{\text{strong}}\rangle . \tag{15}$$

Exact numerical calculations in small lattice sizes $L \leq 8$ confirm that the overlap $|\langle \Psi_{\text{strong}}| E_0\rangle|^2 \gtrsim 0.9$ with the exact ground state is large.

The ground state is expected to be a singlet, while the first excited state is anticipated to possess the quantum numbers of the σ-model particle, namely, a triplet state. Consequently, the operator d must be a component of a vector operator. Given the form of $|\Psi_{\text{strong}}\rangle$ in Eq. (11), we expect the fuzz and head qubits to be treated symmetrically. We find that the operator[4]

$$d_s = \sum_{l=0}^{L-1} (-1)^l [Z_{2l+1} \otimes \mathbb{1}_{2l} - \mathbb{1}_{2l+1} \otimes Z_{2l}], \tag{16}$$

connects $|E_0\rangle$ and $|E_1\rangle$ with significant probability. The initial state is prepared by evolving $|\Psi_{\text{strong}}\rangle$ by the unitary $U = \exp(-id_s t_{\text{prep}})$:

$$|\Psi(0)\rangle = e^{-id_s t_{\text{prep}}} |\Psi_{\text{strong}}\rangle , \tag{17}$$

with a small enough t_{prep} such that the contamination from other excited states is minimized. After that, $|\Psi(0)\rangle$ is evolved by the Hamiltonian in Eq. (10). It is important to notice that not starting from the exact ground state and/or using an imperfect dipole operator $d_s \approx d$ does not lead to a change in the measured oscillation frequency. Instead, those imperfections pollute the ideal form Eq. (14) with higher frequencies. If a long time series is available, these frequencies can be separated by Fourier analysis or other methods. Using the current computers where long time series are impossible due to noise/decoherence, is one of the challenges of this method.

In the weak coupling regime $g \lesssim 0.7$, the ground state can be approximated by $|\Psi_{\text{weak}}\rangle$ (Eq. (12)). We know that the first excited state lies mostly in the subspace

---

[4] For $L = 4$, one would have $d_s = (ZI - IZ)IIIIII - II(ZI - IZ)IIII + IIII(ZI - IZ)II - IIIIII(ZI - IZ)$.

spanned by $|\text{antiferro}\rangle \otimes |\text{any}\rangle$ and the operator connecting it to the first excited state should be a triplet since the ground state is a singlet and the first excited states form a triplet. A simple operator satisfying these conditions is:

$$d_w = \sum_{l=0}^{L-1} (-1)^l Z_{2l+1} . \tag{18}$$

Again, the initial state is prepared as:

$$|\Psi(0)\rangle = e^{-id_w t_{\text{prep}}} |\Psi_{\text{weak}}\rangle , \tag{19}$$

for a sufficiently small t_{prep}, evolved it by the full Hamiltonian in Eq. (10) and the expectation value of d_w computed at different times t. In the weak coupling limit, the approximate dipole operator d_w has non-negligible transition between the ground and many higher excited states. However, the gap $E_1 - E_0$ still dominates the oscillations that can be estimated with appropriate filtering of the oscillations.

IV. CIRCUITS FOR QUANTUM COMPUTATION

The implementation of the algorithm above requires state preperation and the translation of the unitary operators into a set of quantum gates.

We start with the strong coupling limit. The state $|\Psi_{\text{strong}}\rangle$ is a tensor product of the singlet Bell states comprized of the head and fuzz qubits. The singlet state $(|0_{2l+1}1_{2l}\rangle - |1_{2l+1}0_{2l}\rangle)/\sqrt{2}$ can be created by the circuit in Fig. 2 , where the Hadamard gate H
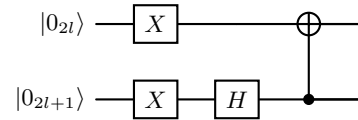

FIG. 2. Circuit for the singlet Bell state. Wires represent the head ($2l$) and fuzz ($2l + 1$) qubits for the site l. H is the Hadamard gate.

$$H \doteq \frac{1}{\sqrt{2}} \begin{bmatrix} 1 & 1 \\ 1 & -1 \end{bmatrix} , \tag{20}$$

is the Hermitian and unitary matrix that diagonalizes $X = HZH$.

The preparation of the initial state $|\Psi(0)\rangle$ and its time evolution to $|\Psi(t)\rangle$ requires the unitary evolution of states involving multiple qubits. This is implemented by applying a sequence of 1- and 2-qubit gates to the multiqubit gates after decomposing the unitary operations into smaller circuits as we will now show.

A Hermitian operator M can be decomposed into a sum of Pauli strings P_is such that $M = \sum_i c_i P_i$ with

$c_i \in \mathbb{R}$. We have already done this for the Hamiltonian H, and the dipole operators d_s and d_w. The time evolution for a small time step Δt is decomposed using the first order Lee-Suzuki-Trotter approximation [40]

$$e^{i\Delta t M} = e^{i\Delta t \sum_j c_j P_j} = \prod_j e^{ic_j \Delta t P_j} + \mathcal{O}(\Delta t^2), \quad (21)$$

whereby the unitary evolution due to the Pauli strings P_is can be applied sequentially. A second order approximation with a smaller error $\mathcal{O}(\Delta t^3)$ is available, however, it nearly doubles the number of quantum gates which is not desirable on the noisy machines currently available. Notice, the Pauli strings in both d_s and d_w commutes, and thus Eqs. (17), (19) incur no error in their Trotterizations. A longer time evolution is constructed by applying the Δt operations multiple times. The constructions of the gates for $\exp(i\Delta t P_j)$ is straightforward since in our calculation the Pauli strings P_js contain at most two Pauli matrices. Implementing $\exp(-id_s\Delta t)$ only requires applying the 1-qubit $R_Z(\theta) = \exp(-i\theta Z/2)$ gate with appropriate θ on the corresponding qubit. This gate is natively available on both the IonQ-Forte and IBMQ-Fez that we used in our calculations. The weak coupling dipole operator d_w also can be implemented with the R_Z gate. We need 2-qubit gates only for the unitary time evolution with the Hamiltonian. The gate $R_{ZZ}(\theta) = \exp(-i\theta Z \otimes Z/2)$ is native on the IonQ machines and, in combination with the Hadamard and the phase gate

$$S \doteq \begin{bmatrix} 1 & 0 \\ 0 & i \end{bmatrix}, \quad (22)$$

generate R_{XX} and R_{YY} through the use of the identities $X = HZX$ and $Y = SHZHS^\dagger$. On the IBMQ-Fez machine, $R_{ZZ}(\theta)$ is available natively as a fractional gate for $\theta \le \pi/2$. The R_{XX}, R_{YY} and R_{ZZ} gates can also be implemented as the circuit shown in Fig. 3 [41]

The final ingredient we need is measurement of the dipole operator once we created the state $|\Psi(t)\rangle$. The dipole operators d_s, d_w are composed of sums of Pauli strings that commute trivially since they are composed of identical Pauli matrices acting on different qubits. Thus, the expectation value of the entire sum of Pauli strings can be done by measuring the qubits in the Z (computational) basis. The expectation value

$$\langle \Psi(t) | Z_l | \Psi(t) \rangle = \langle q_l(t) | Z_l | q_l(t) \rangle$$
$$= P[q_l(t) = 0] - P[q_l(t) = 1], \quad (23)$$

where we only need to take the difference in the probabilities $P(q_l)$ in the measurement of the $|0_l\rangle$ and $|0_l\rangle$ states for all qubits with appropriate phases for d_s and d_w in Eq. (16) and Eq. (18), respectively.

V. RESULTS AND DISCUSSIONS

We separate the discussion of the strong coupling and weak coupling results for clarity. We quote numerical results in lattice units, that is, we scale dimensionful quantities by appropriate powers of lattice spacing a and write them as dimensionless in the rest of the paper.

A. Strong coupling measurements

We performed several calculations on IonQ-Forte and IBMQ-Fez for box sizes from $L = 4$ to $L = 20$ at coupling $g = 1.2$. We prepared the initial state for the time evolution using Eq. (11), Eq. (17) and $t_{\text{prep}} = 0.1$. The time evolution was performed with a Trotter step $\Delta t = 0.4$. This choice is a compromise between being able to resolve the dynamics of the model at a scale $\approx a$ and the need to minimize the number of Trotter steps to reduce noise. We made 1000 measurements at each time step, enough to make the statistical noise less important than all other approximations.

TABLE I. Data from IonQ-Forte, IBMQ-Fez Quantum Processor Unit (QPU) and ideal simulator ($L = 12$). The parameters A, γ, ω were obtained from fits to total time $t = 5.2$ at intervals of $\Delta t = 0.4$. We use lattice untis.

L	A	γ	ω	QPU
4	$-3.97(17)$	$0.544(31)$	$2.64(3)$	IonQ
6	$-5.45(23)$	$0.663(36)$	$2.73(4)$	IonQ
8	$-7.49(23)$	$0.534(23)$	$2.62(2)$	IonQ
12	$-9.83(21)$	$0.204(9)$	$2.54(1)$	IonQ
8	$-6.80(23)$	$0.536(25)$	$2.48(3)$	IBMQ
16	$-13.12(50)$	$0.975(45)$	$2.53(5)$	IBMQ
20	$-17.47(85)$	$1.323(72)$	$2.41(7)$	IBMQ
12	$-9.87(17)$	$0.021(6)$	$2.38(1)$	Ideal

The resulting measurements at the larger lattices $L = 12, 16$ and 20 are shown in Fig. 4. The data exhibits clear oscillatory behavior, dominated by a single frequency. Furthermore, a pronounced damping of the amplitude is apparent.

There are three reasons why this oscillation does not have the pure sinusoidal form in Eq. (14). First, our initial state is not an exact linear combination of ground and first excited states and the contamination of other states with their corresponding frequencies is to be expected. Second, the time evolution contains Trotterization errors due to the finite value of Δt. Finally, current devices are not error corrected and suffer from noise and decoherence errors. Simulations of the same calculation in classical computers and $L \le 10$, which include Trotter errors and the contamination of excited states, show no sign of damping. Therefore, we attribute the damping shown in Fig. 4 to noise and decoherence of the quantum devices we used.

A fit of the ideal simulation results to a damped sinusoidal form

$$\langle d \rangle = Ae^{-\gamma t} \sin(\omega t), \quad (24)$$

gives the values in Table I. The errors shown in Table I
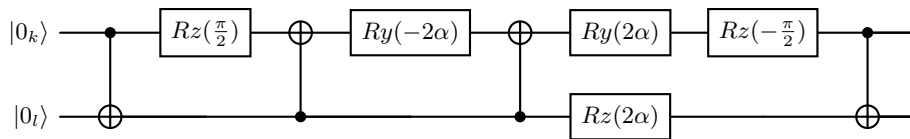
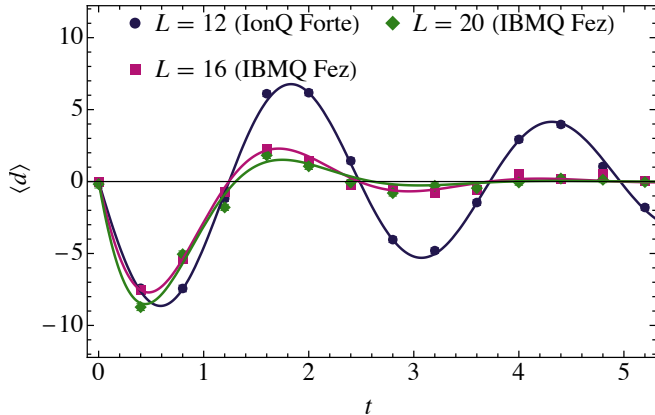FIG. 3. Circuit for $\exp[-i\alpha(X_l X_k + Y_l Y_k + Z_l Z_k)]$.

FIG. 4. Fits to QPU data. Only the largest 3 lattice box sizes shown. The complete set of fits is in Table I. Data up to $t = 5.2$ were used in the fits.

reflect only the quality of the fit to Eq. (24) and the uncertainty due to the finite number of shots. The quality of these fits are exemplified by the solid lines in Fig. 4. The goodness of the fit is another indication that, at least for the parameters considered, there is very little contamination of excited states outside the subspace spanned by $|E_0\rangle, |E_1\rangle$. This is true despite the fact that neither $|\Psi_{\text{strong}}\rangle$ equals the exact ground state $|E_0\rangle$ nor that $d|E_0\rangle$ equals the exact excited state $|E_1\rangle$. Simulations in classical computers show that the contamination from excited states would be very apparent if larger values of t_{prep} were used and this guided our choice of t_{prep}.

The fitting function in Eq. (24) fits the data fairly well but is arbitrary. Therefore, the identification of ω appearing in Eq. (24) with the mass gap m introduces an uncontrolled error arising from this arbitrariness. The dependence of the mass gap m with the volume is known to be suppressed by $\sim e^{-mL}$ in the $mL \to \infty$ limit [42]. The values of ω shown in Table I are clearly in this regime and, therefore, we do not expect a noticeable volume dependence on the value of the gap. The slight discrepancy between the values of ω in Table I should then be ascribed to the uncontrolled errors due to the arbitrary form in Eq. (24) and serve as a measure of this uncertainty. The average of ω over the different values of L from the Quantum Processor Unit runs results in $\omega = 2.56(2)$, where the error is given by the spread in the values in Table I. Attempts to reduce and quantify the Trotterization errors by performing calculations at smaller Trotter steps Δt turned out to be impossible due

to the significant increase of noise/decoherence errors as the number of Trotter steps increases.

If we identify ω in Eq. (14) with the gap $m = E_1 - E_0$ we find a discrepancy from the correct value $m_{exact} \approx 2.34$ obtained from direct diagonalization in lattices $L \leq 12$ (the finite volume effect beyond $L = 10$ are negligible) of about 9%. As we will see below, a noiseless calculation, for which Eq. (24) is adequate, eliminates this discrepancy.

B. Weak coupling analysis

The weak coupling limit, which includes the scaling region near the continuum limit, presents a different kind of challenge. Near the continuum limit the gap is very small (in lattice units) and the oscillation very slow. Therefore, one needs to compute $\langle d \rangle$ to much larger times. However, in order to capture the high momentum modes correctly, the Trotter step size Δt has to remain small. Consequently, the number of Trotter steps required is much larger. In an error corrected machine this would lead to a moderate cost increase, linear on the inverse gap. In a noisy machine, however, a large number of Trotter steps means a large number of gates and the dilution of the signal by noise/decoherence before any meaningful results can be extracted. Alternatively to Trotter, other simulation algorithms, such as the quantum signal processing (QSP) [43], scale better but are prohibitive on current noisy hardware. For this reason, we demonstrate the feasibility of the general algorithm in an ideal (noiseless) simulation in Fig. 5 at $g = 0.6$ using the Trotter decomposition for simplicity.

The weak coupling calculation requires a few additional considerations. As the coupling gets smaller and the correlation lengths larger, the finite volume corrections become more noticeable: whereas at the strong coupling $g = 1.2$, the gap varies from $\omega = 2.3368$ at $L = 4$ to $\omega = 2.3370$ at $L = 10$; at weak coupling $g = 0.6$, we find the gap varies from $\omega = 0.054098$ at $L = 4$ to $\omega = 0.042759$ at $L = 10$. Usually, larger volume simulations would be desirable for $L \to \infty$ extrapolations using Lüscher method. The initial state $|\Psi(0)\rangle$ preparation from $|\Psi_{\text{weak}}\rangle$ also requires some deliberation. We
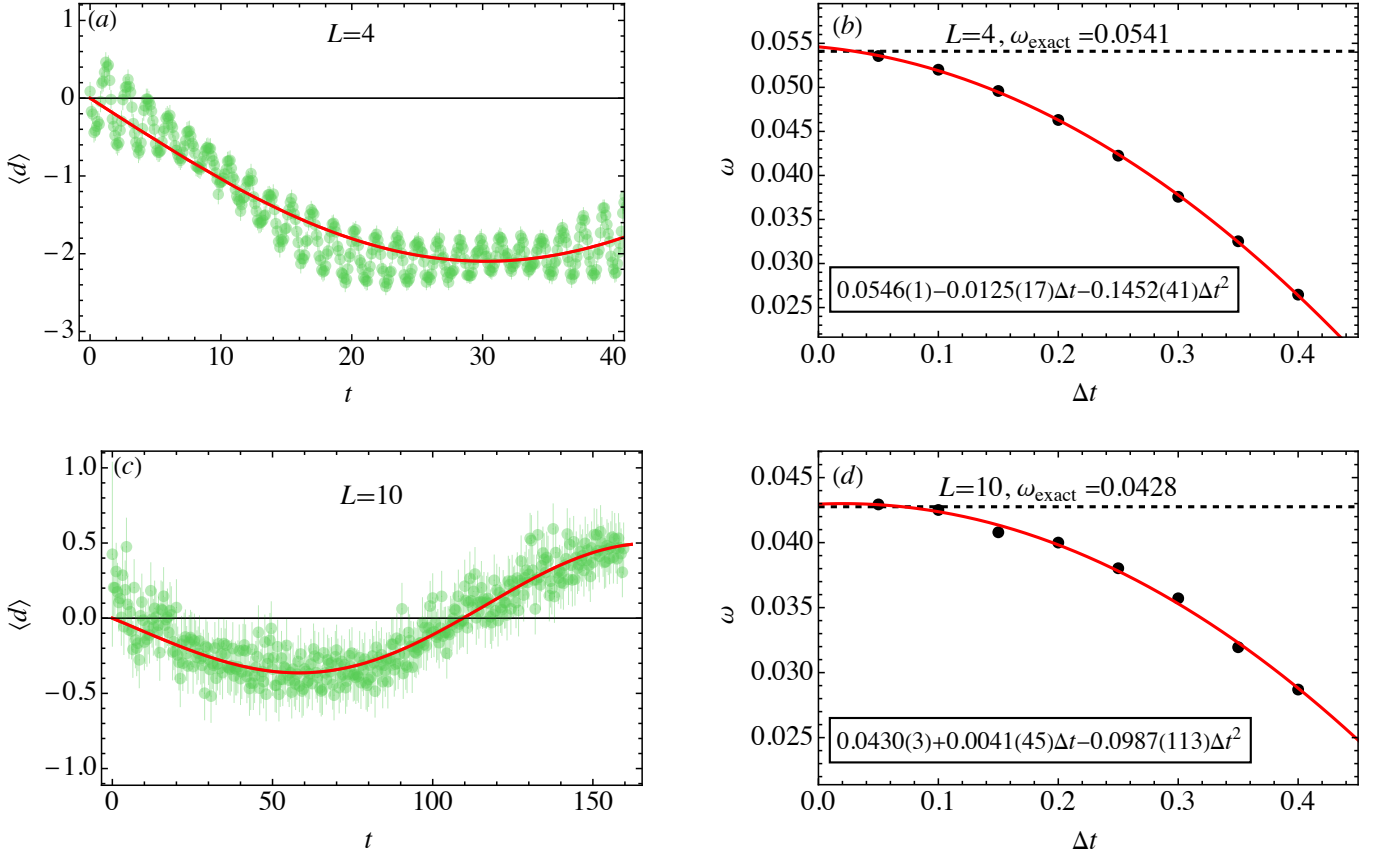
FIG. 5. Top left panel: Large volume $L = 4$ ideal simulation data (green data points) for $\langle d \rangle$ vs time t at weak coupling $g = 0.6$ with $\lambda = 0.5$ in Eq. (25), $t_{\text{prep}} = 0.1$, and Trotter steps $\Delta t = 0.1$. The solid (red) curve is a fit of the form in Eq. (24) whose fit parameters are provided in the text. Top right panel: Extrapolation of the gap ω to $\Delta t \to 0$ for $g = 0.6$, $L = 4$. The (black) data points are the gaps extracted from ideal simulations at Δt values as indicated. The solid (red) curve is a polynomial fit whose coefficients are indicated in the boxed insert. The extracted value $\omega = 0.054\,61(10)$ is to be compared with the exact numerical result $\omega_{\text{exact}} = 0.0541$. We have indicated only the errors from the χ^2 fit. As discussed in the text, a cubic Δt^3 term in the fit brings the extracted ω value in better agreement with the exact result. Bottom left panel: Large volume $L = 10$ ideal simulation data (green data points) for $\langle d \rangle$ at weak coupling $g = 0.6$ with $\lambda = 0.1$ in Eq. (25), $t_{\text{prep}} = 0.01$, and Trotter steps $\Delta t = 0.4$. Rest of the notation is the same as the top left panel. The solid (red) curve fit parameters are provided in the text. Bottom right panel: Extrapolation of the gap ω to $\Delta t \to 0$ for $g = 0.6$, $L = 10$. Rest of the notation is the same as the top right panel. The solid (red) curve is a polynomial fit with coefficients as indicated in the boxed insert. The extracted value $\omega = 0.0430(3)$ is in agreement with the exact numerical result $\omega_{\text{exact}} = 0.0428$. We have indicated only the errors from the χ^2 fit.

construct a dipole operator

$$d(\lambda) = \lambda d_s + (1 - \lambda)d_w$$
$$= \sum_{l=0}^{L-1} (-1)^l [Z_{2l+1} \mathbb{1}_{2l} - \lambda \mathbb{1}_{2l+1} Z_{2l}], \quad (25)$$

from a simple linear extrapolation between the strong and weak coupling limits. Further, we take a smaller t_{prep} when L is larger to reduce the contamination from the higher excited states to which d_w couples.

We perfom a small $L = 4$ and a large $L = 10$ volume calculation at weak coupling $g = 0.6$ to illustrate what has been discussed above, see Fig. 5. At $L = 4$, we prepare the initial state $|\Psi(0)\rangle$ using $t_{\text{prep}} = 0.1$ and $\lambda =$

0.5 with Trotterization steps $\Delta t = 0.05$ to 0.4 in intervals of 0.05. The contamination from higher excited states in Fig. 5 (a) for the $\Delta t = 0.1$ result is visible as fast oscillations on top of the dominant feature due to the low frequency oscillations from the vanishing energy gap $E_1 - E_0$. We fit the form in Eq. (24) and find $A = -2.10(2)$, $\omega = 0.052\,00(5)$ with a vanishing $\gamma = -9.6(82) \times 10^{-5}$ damping exponent, indicating the sinusoidal nature of the signal.

The larger volume $L = 10$ calculation in Fig. 5 was performed with an initial state $|\Psi(0)\rangle$ prepared with a much shorter $t_{\text{prep}} = 0.01$ and smaller $\lambda = 0.1$ to eliminate contamination from higher excited state. As the volume increases, the energy levels shift downward at different rates, decreasing the relative gaps between states in the

process. A shorter t_{prep} and smaller λ becomes necessary to obtain a dominant sinusoidal form. A consequence of shorter t_{prep} is smaller overlap between the ground and excited states though one can still obtain the desired signal. We find a fit to simulation data using Eq. (24) gives $A = -0.309(14)$, $\gamma = -0.0029(4)$, $\omega = 0.0287(2)$ at $\Delta t = 0.4$. In Fig. 5 (c), we show results for $\Delta t = 0.4$ instead of $\Delta t = 0.1$ at $L = 10$ for visualization as the latter would have four times as many data points in the same time interval. We also mention that both the $L = 4$ and $L = 10$ data were fit over the same time interval of $t = 160$. Fig. 5 (a) is zoomed in over a shorter time interval to highlight the fast oscillations.

In Fig. 5, right panels, we show extrapolations of ideal simulation data to $\Delta t \to 0$. At $L = 4$, a quadratic polynomial fit gives an extrapolated gap $\omega = 0.0546(1)$ that changes to $\omega = 0.0542(1)$ when a cubic Δt^2 term is added. This is to be compared to $\omega_{\text{exact}} = 0.0541$. A similar fit at $L = 10$ gives an extrapolated gap $\omega = 0.0430(3)$ in good agreement with the exact numerical result $\omega_{\text{exact}} = 0.0428$. Adding a cubic term changes the fitted value slightly to $\omega = 0.0435(6)$. All the quoted errors here are from the fits only.
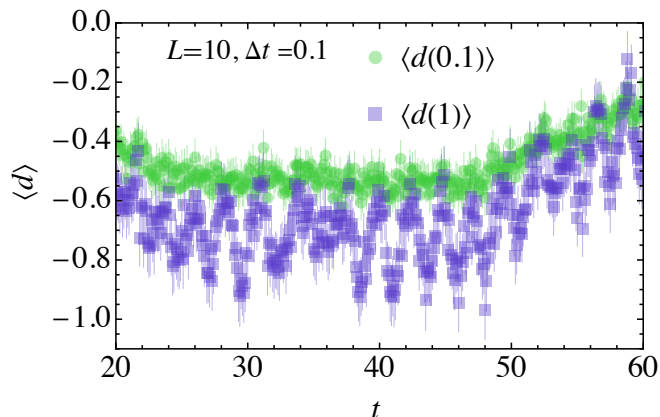

FIG. 6. Measurement of dipole operators $d(\lambda = 0.1)$ and $d(\lambda = 1)$ using the same state $|\Psi(t)\rangle$ prepared from $|\Psi(0)\rangle = \exp[-it_{\text{prep}} d(0.1)]|\Psi_{\text{weak}}\rangle$ with $t_{\text{prep}} = 0.1$ and $\Delta t = 0.1$ at $g = 0.6$ and $L = 10$.

Before concluding, we make the following observation. The algorithm we presented (for both strong and weak coupling) involves several distinct steps. First, we prepare the initial state $|\Psi(0)\rangle$ with an unitary evolution with a dipole operator for time t_{prep}. The form of the dipole operator whether d_s, d_w or some linear combination of these allows error free Trotterization since each Pauli strings in the dipole operators mutually commute. However, as discussed earlier, the choice of t_{prep} depends on the size of the coupling g, with a smaller t_{prep} at weaker couplings to reduce contamination from higher excited states. The second step involves unitary evolution with the system Hamiltonian which incurs Trotterization errors. Thus, one has to balance the Trot-

ter steps Δt with the circuit depth especially at weak couplings where a longer total time evolution becomes necessary for the vanishing gap. The final step involves measurement of the dipole operator. The only necessary condition to produce the oscillations used in the gap calculation is that we pick an observable/operator that does not commute with the Hamiltonian (and that the initial state is a linear superposition of energy eigen states). In particular, it means we do not have to measure the same dipole operator that was used in the state preparation. In Fig. 6 we show the expectation values of two different dipole operator using the same exact initial state preparation. We emphasize that this does not require separate quantum simulation. The same simulation can be used for measurement of multiple observables, at post processing. For example, in our algorithm, we produced the initial state $|\Psi(0)\rangle$ at $g = 0.6$, $L = 10$ with $d(\lambda = 0.1)$ and $t_{\text{prep}} = 0.1$ and evolved the system with $\Delta t = 0.1$ and recording the state $|\Psi(t)\rangle$ at later time t (in computational basis). We used 10,000 shots to improve precision in the ideal simulation. Then we can measure multiple observables $\langle A \rangle$, $\langle B \rangle$, etc. with the same $|\Psi(t)\rangle$. In Fig. 6, the green data points corresponds to measurement of $d(\lambda = 0.1)$ where the contamination from the higher excited states are washed out. A fit of the form in Eq. (24) gives $\omega = 0.042\,96(3)$. The purple data points are from measurement of $d(\lambda = 1)$ that couples strongly to some of the higher excited state resulting in the higher frequency oscillations on top of the dominant low frequency oscillation. A similar fit to Eq. (24) gives $\omega = 0.042\,68(5)$ in agreement with the earlier green data points. This ability to measure different observables from the same state preparation and unitary time evolution is not a shortcoming but an advantage. It can be used to highlight different aspect of the physical system.

VI. CONCLUSION

The results presented here demonstrate a viable method for calculating the mass spectrum in a field theory using quantum computers. By constructing an operator that couples the lowest energy states with two different quantum numbers and tracking the time evolution of its expectation value, we can extract the mass gap from the oscillation frequency. Using exact diagonalization on small lattices, we verified this approach and then extended it to larger systems beyond classical computational reach.

Our method was shown to work for lattice sizes up to $L = 20$, corresponding to a Hilbert space of dimension 2^{40}, well beyond the capacity of direct diagonalization in a classical computater. Although the signal becomes increasingly damped with system size, as long as the gap remains sufficiently large, the oscillation frequency can still be accurately fitted. In the continuum/scaling region at weak coupling, the oscillations become slower and the signal decays before a complete oscillation in $\langle d \rangle$ can

be observed. In this regime, better, error corrected computers would be required to apply our method.

Overall, this work establishes a proof of concept for probing excitation spectra and real-time dynamics in lattice field theories using quantum devices. Demonstrating simulations of systems with Hilbert spaces far exceeding classical limits represents a significant step toward leveraging quantum hardware for nonperturbative field theory calculations.

[1] T. Byrnes and Y. Yamamoto, Simulating lattice gauge theories on a quantum computer, Phys. Rev. A **73**, 022328 (2006).

[2] A. Kan and Y. Nam, Simulating lattice quantum electrodynamics on a quantum computer, Quantum Sci. Technol. **8**, 015008 (2023).

[3] A. Kan and Y. Nam, Lattice Quantum Chromodynamics and Electrodynamics on a Universal Quantum Computer, (2021), arXiv:2107.12769 [quant-ph].

[4] P. Balaji, C. Conefrey-Shinozaki, P. Draper, J. K. Elhaderi, D. Gupta, L. Hidalgo, A. Lytle, and E. Rinaldi, Quantum circuits for SU(3) lattice gauge theory, Phys. Rev. D **112**, 054511 (2025).

[5] E. Zohar, J. I. Cirac, and B. Reznik, Cold-Atom Quantum Simulator for SU(2) Yang-Mills Lattice Gauge Theory, Phys. Rev. Lett. **110**, 125304 (2013).

[6] E. Zohar, A. Farace, B. Reznik, and J. I. Cirac, Digital lattice gauge theories, Phys. Rev. A **95**, 023604 (2017).

[7] E. Zohar and M. Burrello, Formulation of lattice gauge theories for quantum simulations, Phys. Rev. D **91**, 054506 (2015).

[8] A. N. Ciavarella, I. M. Burbano, and C. W. Bauer, Efficient truncations of SU(Nc) lattice gauge theory for quantum simulation, Phys. Rev. D **112**, 054514 (2025).

[9] D. M. Grabowska, C. F. Kane, and C. W. Bauer, Fully gauge-fixed SU(2) Hamiltonian for quantum simulations, Phys. Rev. D **111**, 114516 (2025).

[10] H. Lamm, S. Lawrence, and Y. Yamauchi, General Methods for Digital Quantum Simulation of Gauge Theories, Phys. Rev. D **100**, 034518 (2019).

[11] H. Lamm, Y.-Y. Li, J. Shu, Y.-L. Wang, and B. Xu, Block encodings of discrete subgroups on a quantum computer, Phys. Rev. D **110**, 054505 (2024).

[12] E. J. Gustafson and H. Lamm, Toward quantum simulations of $\mathbb{Z}_2$ gauge theory without state preparation, Phys. Rev. D **103**, 054507 (2021).

[13] E. J. Gustafson, H. Lamm, F. Lovelace, and D. Musk, Primitive quantum gates for an SU(2) discrete subgroup: Binary tetrahedral, Phys. Rev. D **106**, 114501 (2022).

[14] E. J. Gustafson, H. Lamm, and F. Lovelace, Primitive quantum gates for an SU(2) discrete subgroup: Binary octahedral, Phys. Rev. D **109**, 054503 (2024).

[15] M. S. Alam, S. Hadfield, H. Lamm, and A. C. Y. Li (SQMS), Primitive quantum gates for dihedral gauge theories, Phys. Rev. D **105**, 114501 (2022).

[16] E. M. Murairi, M. Sohaib Alam, H. Lamm, S. Hadfield, and E. Gustafson, Highly-efficient quantum Fourier transformations for certain non-Abelian groups, Phys. Rev. D **110**, 074501 (2024).

[17] E. J. Gustafson, Y. Ji, H. Lamm, E. M. Murairi, S. O. Perez, and S. Zhu, Primitive quantum gates for an SU(3) discrete subgroup: $\Sigma(36\times3)$, Phys. Rev. D **110**, 034515 (2024).

[18] S. O. Perez, E. M. Murairi, E. J. Gustafson, and H. Lamm, Primitive Quantum Gates for an $SU(3)$ Discrete Subgroup: $\Sigma(72 \times 3)$, (2025), arXiv:2511.17437 [hep-lat].

[19] A. Alexandru, P. F. Bedaque, A. Carosso, M. J. Cervia, and A. Sheng, Qubitization strategies for bosonic field theories, Phys. Rev. D **107**, 034503 (2023).

[20] A. Alexandru, P. F. Bedaque, A. Carosso, and A. Sheng, Universality of a truncated sigma-model, Phys. Lett. B **832**, 137230 (2022).

[21] A. Alexandru, P. F. Bedaque, A. Carosso, M. J. Cervia, E. M. Murairi, and A. Sheng, Fuzzy gauge theory for quantum computers, Phys. Rev. D **109**, 094502 (2024).

[22] T. V. Zache, M. Van Damme, J. C. Halimeh, P. Hauke, and D. Banerjee, Toward the continuum limit of a $(1 + 1)$D quantum link schwinger model, Phys. Rev. D **106**, L091502 (2022).

[23] S. Chandrasekharan and U.-J. Wiese, Quantum link models: A discrete approach to gauge theories, Nuclear Physics B **492**, 455 (1997).

[24] U.-J. Wiese, From quantum link models to D-theory: a resource efficient framework for the quantum simulation and computation of gauge theories, Phil. Trans. A. Math. Phys. Eng. Sci. **380**, 20210068 (2021).

[25] A. Alexandru, P. F. Bedaque, H. Lamm, and S. Lawrence (NuQS), σ Models on Quantum Computers, Phys. Rev. Lett. **123**, 090501 (2019).

[26] H. Singh and S. Chandrasekharan, Qubit regularization of the $O(3)$ sigma model, Phys. Rev. D **100**, 054505 (2019).

[27] T. Bhattacharya, A. J. Buser, S. Chandrasekharan, R. Gupta, and H. Singh, Qubit regularization of asymptotic freedom, Phys. Rev. Lett. **126**, 172001 (2021).

[28] J. Zhou, H. Singh, T. Bhattacharya, S. Chandrasekharan, and R. Gupta, Spacetime symmetric qubit regularization of the asymptotically free two-dimensional O(4) model, Phys. Rev. D **105**, 054510 (2022).

[29] F. Bruckmann, K. Jansen, and S. Kühn, O(3) nonlinear sigma model in $1 + 1$ dimensions with matrix product states, Phys. Rev. D **99**, 074501 (2019).

[30] A. Polyakov, Interaction of goldstone particles in two dimensions. applications to ferromagnets and massive yang-mills fields, Physics Letters B **59**, 79 (1975).

[31] A. B. Zamolodchikov and A. B. Zamolodchikov, Relativistic factorized s-matrix in two dimensions having o(n) isotopic symmetry, Nuclear Physics B **133**, 525 (1978).

[32] S. Caracciolo, A. Montanari, and A. Pelissetto, Asymptotically free models and discrete non-abelian groups, Phys. Lett. B **513**, 223 (2001).

[33] A. Patrascioiu and E. Seiler, Is the 2D $O(3)$ nonlinear σ model asymptotically free?, Phys. Lett. B **430**, 314 (1998).

[34] P. Hasenfratz and F. Niedermayer, Asymptotic freedom with discrete spin variables?, PoS **HEP2001**, 229 (2001).

[35] J. Hoppe, Membranes and matrix models, arXiv:hep-th/0206192.

[36] J. Madore, The Fuzzy sphere, Classical Quantum Gravity **9**, 69 (1992).

[37] H. Singh and S. Chandrasekharan, Qubit regularization of the $O(3)$ sigma model, Phys. Rev. D **100**, 054505 (2019).

[38] H. Liu and S. Chandrasekharan, Qubit Regularization and Qubit Embedding Algebras, Symmetry **14**, 305 (2022).

[39] M. Douglas and N. Nekrasov, Noncommutative field theory, Reviews of Modern Physics **73**, 977–1029 (2001).

[40] M. Suzuki, General theory of fractal path integrals with applications to many-body theories and statistical physics, Journal of Mathematical Physics **32**, 400 (1991).

[41] F. Vatan and C. Williams, Optimal quantum circuits for general two-qubit gates, Phys. Rev. A **69**, 032315 (2004).

[42] M. Luscher, Volume Dependence of the Energy Spectrum in Massive Quantum Field Theories. 1. Stable Particle States, Commun. Math. Phys. **104**, 177 (1986).

[43] G. H. Low and I. L. Chuang, Optimal hamiltonian simulation by quantum signal processing, Phys. Rev. Lett. **118**, 010501 (2017).